Journal of Materials Research and Technology 30 (2024) 8080–8091

Contents lists available at ScienceDirect

Journal of Materials Research and Technology

journal homepage: www.elsevier.com/locate/jmrt

The ablation behavior and modification mechanism of SiC under different laser energy

Zhipeng Li [a,*], Mengmeng Jin [a], Haixu Liu [a], Dunwen Zuo [a], Wenkun Xie [b]

[a] NanJing University of Aeronautics and Astronautics, Nanjing, 210016, China
[b] Department of Design, Centre for Precision Manufacturing, Manufacturing & Engineering Management University of Strathclyde, Glasgow, United Kingdom

ARTICLE INFO

Handling editor: L Murr

ABSTRACT

The laser modification pretreatment method is an effective way to address the machining difficulties of silicon carbide (SiC), a typical hard-to-machine material. Therefore, the ablation behavior and modification mechanism of SiC under different laser energy were explored in this paper. A new multi-scale model of laser irradiation SiC that couples heat transfer and fluid motion is first established. Then, a series of experiments is carried out to evaluate the model's accuracy, and the interaction between laser and SiC is discussed in detail. The results show that the dominant modification mechanism changes from coulomb explosion to multiphoton absorption, incubation effect, and heat accumulation with the laser energy increase. This leads the surface topography of SiC to transition from nanoparticle formation to disorder to a melting state. In ablative state, micro/nano porous and humps are formed at the edge of ablation groove due to surface tension, generation and rupture of bubbles, respectively. Furthermore, the surface roughness is not proportional to the laser energy due to the plasma shielding effect, and the surface roughness can be reduced by enhancing the flow of the molten material. Amorphous Si–O–C, Si and spherical SiO_2 exist in deposition area, leading to SiC elastic modulus decreases from 347 GPa to 103.82 GPa, and the shear strength decreases from 20.9 GPa to 17.25 GPa. The results of this study can provide references for parameters selection and theoretical support for improving the machinability of SiC.

1. Introduction

Due to its unique characteristics such as a wide band gap, high critical breakdown field strength and thermal conductivity, SiC has become an advanced material in semiconductor and aerospace industries. Particularly in harsh environments, its ability to maintain the stable performance has earned favor among manufactures [1]. However, its high hardness (Mohs hardness of 9.5), low fracture toughness and chemical stability lead SiC extremely difficult to machine. Cracks, lateral damages, extrusion fracture, and delamination are inevitably induced during the machining processes, which is a key factor affecting the fatigue life of SiC components. Although researchers discovered the advantages of SiC materials as early as the 1960s, the issues of poor machinability and high defect density have yet to be resolved. For those reasons, SiC substrates are not only expensive but also difficult to use for producing high-quality and large-size SiC wafers [2].

The precision processing of SiC substrates mainly involves three stages: slicing, grinding, and polishing. Among these, polishing is a key step that determines the quality of epitaxial thin films and device performance. The purpose of polishing is to eliminate the surface and sub-surface defects caused by the growth and cutting of single-crystal SiC wafers, in order to achieve a defect-free and atomic-level ultra-precision surface. To achieve high-efficiency and high-precision polishing of SiC, numerous scholars have conducted extensive research and exploration on hybrid polishing process. Yamamura et al. [3] utilized argon-based plasma containing water vapor to assist in PAP single-crystal diamond polishing, the MRR of 2.1 μm/h, the surface roughness of 0.13 nm (Sq) was obtained. However, implementing this technique requires complex equipment systems and high fixed costs. Deng et al. [4] introduced an electrochemical mechanical polishing (ECMP) technique that combines anodization and soft abrasives. This method reduces the surface hardness of SiC from 34.5 GPa to 1.9 GPa, enabling the use of very soft abrasives like CeO_2 to polish oxidized SiC surfaces. With this method, a smooth surface with a root mean square roughness of 0.23 nm can be achieved, and the material removal rate can reach 3.62 μm/h. However, the uneven oxidation of the workpiece surface makes the process challenging to control. Zhu et al. [5] employed magnetorheological polishing (MRF) to process silicon

* Corresponding author.
E-mail address: zhipeng.li@nuaa.edu.cn (Z. Li).

https://doi.org/10.1016/j.jmrt.2024.05.125
Received 14 April 2024; Received in revised form 13 May 2024; Accepted 14 May 2024
Available online 15 May 2024

carbide, using H_2O_2 as an oxidant to enhance the chemical reaction on the workpiece surface. They obtained an ultra-smooth surface at the atomic level, reducing the wafer roughness Ra from 50.86 nm to 0.42 nm, with a material removal rate of 98 nm/min. However, this method is sensitive to the distance between the magnetorheological fluid and the workpiece, and the discharge of the oxidant may lead to environmental pollution. Hybrid polishing techniques combine chemical etching and mechanical effects, offering new possibilities for the precision polishing of hard-to-machine materials [6]. However, balancing these two effects remains a challenge in achieving an efficient, smooth, and damage-free SiC surface.

As a non-contact machining method, ultra-fast laser machining has a series of advantages, including excellent controllability, producing less damage and a small heat-affected zone. In 1965, Birnbaum [7] observed a series of periodic ripples on the surface of semiconductor materials after irradiating semiconductor them with linearly polarized long-pulse lasers, which were later called Laser-Induced Periodic Surface Structures (LIPSS). The formation of LIPSS alters the surface micro-morphology and composition of the material. When compared with the SiC matrix, LIPSS exhibits lower strength and hardness [8], which is beneficial for the polishing process. LIPSS is categorized into low spatial frequency LIPSS (LSFL) and high spatial frequency LIPSS (HSFL) based on the period. The period of HSFL is much smaller than the incident light wavelength ($\lambda/6 - \lambda/4$) [9]. Obara et al. [10] studied the evolution of high spatial frequency ripples (HSFL) produced by femtosecond laser irradiation on the surface of SiC crystals and proposed that the reason for HSFL is Mie scattering. Molian et al. [11] used a picosecond laser to ablate 4H–SiC wafers. The grooves and holes processed exhibited clean and smooth walls. When the laser repetition rate exceeded 500 KHz, carbonaceous materials and recast layers appeared in the processing area. They attribute the phenomenon to the interaction between air plasma and nanoparticles, suggesting that the material removal mechanism is based on the Coulomb explosion. Wang et al. [12] experimentally employed a femtosecond laser to pretreat SiC, resulting in a threefold increase in the CMP efficiency of SiC. Xie et al. [13] investigated the effect of the processing environment on the laser-machined surface and demonstrated that an oxygen environment can lead to fewer surface defects and lower surface roughness. Softening of SiC materials using laser irradiation can significantly improve CMP efficiency, as confirmed by previous studies. Therefore, it can be inferred that resolving the issue of low polishing efficiency in SiC materials hinges on inducing uniform and continuous LIPSS on the SiC surface while controlling the thickness of the defect layer. Due to the non-contact nature of ps-pulsed lasers, directly obtaining transient temperature and velocity distributions experimentally is challenging [14]. Consequently, numerical simulation is essential for analyzing the temperature evolution during laser ablation and the material removal mechanism. Sciti et al. [15] presented microstructural surface modification of SiC as a function of laser processing parameters, but did not account for physical phenomena such as recoil pressure, energy loss due to evaporation loss. Samant et al. [16] simulated the drilling process of silicon carbide using a nanosecond pulsed Nd: YAG laser, considering the thermal effect of the material, surface tension of the molten part, and energy loss caused by decomposition. The model can predict the drilling depth under specific processing conditions. However, this model focuses on the interaction between the laser and SiC and associated heat transfer properties, with less emphasis on exploring the material removal mechanism and the simulation of the microstructure formation process. In terms of experiments, Wang et al. [17] utilized multi-femtosecond (fs) laser ablation to treat 4H–SiC substrates, studying the evolution of surface topography and the uniformity of the rippled structure but not concentrating on the changes in the mechanical properties of the modified surface. Xie et al. [13] discussed the influence of various laser processing parameters such as femtosecond laser energy density, focus position, scanning speed, and scanning interval on the surface morphology of SiC. On the other hand, Huseynov et al. characterized the thermal properties of SiC nanoparticles using thermogravimetric analysis (TGA) [18]. They noted that SiC exhibits very stable physical properties up to a temperature of 1270 K, with the oxidation rate practically close to zero up to 1000 °C. Subsequently, they investigated the impact of neutron irradiation on the thermal properties of β-SiC nanoparticles [19,20]. It showed that neutron irradiation could induce the nuclear transforms of ^{31}Si to ^{31}P, improving the oxidation resistance of SiC. Moreover, no significant changes were observed in the differential scanning calorimetry (DSC) and TG curves, indicating that SiC nanoparticles possess good radiation-resistant properties. The aforementioned research highlights that the modification of SiC is a challenging task, with laser treatment being one of the more effective methods [21,22]. However, the formation mechanism of the surface microstructure of SiC remains unexplained. Therefore, this paper establishes a multi-scale coupled model of picosecond pulsed laser irradiation on SiC substrate based on heat transfer and fluid motion. The model treats the laser as a bulk heat source and accounts for the influence of the thermal properties of SiC on the transient process. The surface profile predicted by the simulation is compared with the experimental data to validate the proposed mechanism's rationality. The temperature evolution and material removal mechanism during ps laser ablation of SiC are analyzed. In the experiment, various laser processing parameters are employed to scan the SiC surface, and the evolution process of the surface microstructure and the formation mechanism of LIPSS are thoroughly analyzed. Finally, the effect of laser energy influence on the profile after ablation and the alteration of material properties are discussed. The research findings offer valuable insights for a comprehensive understanding of the mechanism behind ps laser modification of SiC. It is poised to propel the practical application of this processing method in industrial production, bringing about new opportunities and challenges for the development of material processing.

2. Theoretical models and simulations

When polishing the modified SiC material, the surface morphology of the material significantly influences the removal rate, roughness, and other indicators. To better control the ablation process, a thorough understanding of the pulsed laser's action mechanism on SiC material is essential, along with quantifying the evolution of the physical fields involved in the ablation process. In this study, the ablation process of SiC by a pulsed laser is simulated under conditions of a 10 ps pulse width and a wavelength of 1030 nm. A multi-scale coupled model is established based on optical carrier absorption, thermal conduction, thermal radiation, and phase transition resolidification process. Within this model, the Fourier heat transfer equation and the N–S equation are used to depict the thermal effects of the laser on the material and the motion of the molten material, respectively. In addition, to more accurately simulate the thermal response of the irradiated material, the model incorporates material properties as a function of temperature and simulates the movement of the vapor/liquid interface during ablation.

2.1. Assumption

- Absorption and defocusing of the laser beam by metal particles, vapor flow, and plasma plume above the ablation region are not considered in this model. This decision is based on the findings of Mao et al. [23], who demonstrated in the related experiments of picosecond laser ablation of metals that almost no plasma can be detected within 20 ps. The influence of the Knudsen layer on the laser ablation process is not taken into account.
- The reflection of the laser beam in the ablated area is not considered in the model. It is assumed that the pulsed laser acts directly impacts the thin layer of fluid near the vapor/liquid interface and can move in real-time with the change of the V/L interface.

- The properties of solid materials are uniform, with mechanical properties being identical in all directions.
- Thermophysical properties and fluid properties of materials are considered as functions of temperature in the model. The fluid in the model treated as an incompressible Newtonian fluid, and the flow state is assumed to be laminar flow.

2.2. Energy absorption and thermal effects

The pulsed laser ablation process can be delineated into the following three stages: 1) Initially, the pulsed laser irradiates the material's surface, leading to a rapid deposition of laser energy. This results in a swift rise in temperature within the target ablation area, causing the material to melt; 2) Subsequently, as the temperature of the liquid phase material continues to escalate, gasification and ionization processes take place, generating a dense, high-temperature vapor stream. Due to the recoil action of the vapor flow, the material in the molten zone overcomes surface tension and gravity, detaching from the material's surface in the form of a vapor/liquid mixture, thereby creating a pit; 3) Once the pulsed laser's influence subsides, the molten liquid residue adhering to the pit's walls will flow back and solidify, resulting in the formation of uneven landforms. During laser irradiation of SiC, the energy delivered by the pulsed laser to the material is the only source of heat. The laser intensity distribution on the material surface is given by:

$$I(r,z=0,t)=\frac{2P}{\pi r_0^2 f\tau}e^{\left(-2\frac{r^2}{r_0^2}\right)}e^{\left(-4\ln 2\left(\frac{(t-\tau)^2}{\tau^2}\right)\right)} \tag{1}$$

where P is the average power of the laser, f is the frequency of the laser beam, which is set to 400 kHz according to the experiment, τ is the pulse width (20 ps), and the spot radius of the laser beam (the distance from the laser center when the intensity drops to $1/e^2$ of the maximum intensity). In the experiment, the laser irradiation direction was perpendicular to the surface of the material, and the spatiotemporal distribution of the laser energy density is shown in Fig. 1. The model uses a body heat source to describe the energy absorbed by the material:

$$Q(r,z,t)=\alpha e^{-\alpha z}(1-R)I(r,z=0,t) \tag{2}$$

where α is the absorption coefficient of SiC for a laser with a wavelength of 1030 nm, and R is the surface reflectance.

The model describes the heating process of the workpiece by the laser based on the Fourier heat transfer law. The equation is as follows:

$$\rho C_p\frac{\partial T}{\partial t}+\rho C_p\vec{\mu}\bullet\nabla T+\nabla q=Q \tag{3}$$

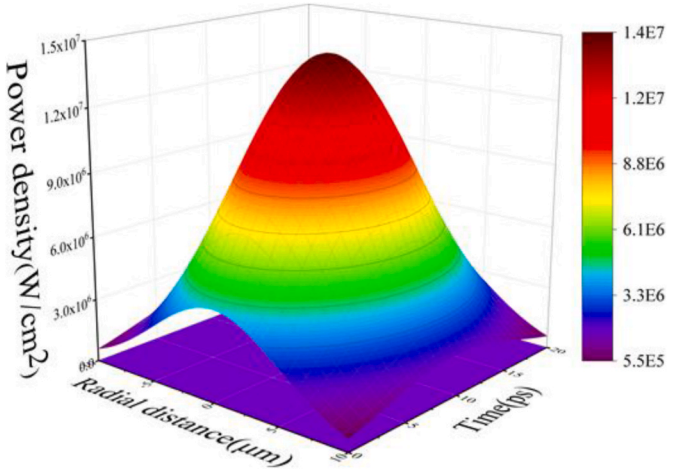

Fig. 1. Spatial and temporal distribution of energy density of laser beam.

$$q=-k\nabla T$$

where ρ is the density of SiC (3100 kg/cm^3 [16]), and k and C_p are the thermal conductivity and constant pressure heat capacity of SiC, respectively. The model takes into account the variation of k and C_p of SiC with temperature (Fig. 2), and they will be regarded as constants when the temperature is greater than 1700 K. This method not only improves the calculation accuracy but also solves the problem of latent heat of phase transition during the heating and cooling of the material.

The vaporization temperature of SiC is 3103K [24]. When the material temperature is higher than this temperature, SiC particles separate from the workpiece surface to form a high-temperature steam flow. This process takes away a large amount of heat. The evaporation rate of the target surface can be expressed as:

$$\dot{m}=P_{sat}(T)\left(\frac{m}{2\pi k_b T}\right)^{\frac{1}{2}}$$

$$P_{sat}(T)=P_0 e^{\Delta H_v\frac{T-T_v}{RTT_v}} \tag{4}$$

where m is the mass of the gaseous SiC molecule ($6.641\times10-26\,kg$), k is the Boltzmann constant, R is the ideal gas constant ($8.314\,J{\cdot}mol^{-1}\,K^{-1}$), T_v is the vaporization temperature. $P_{sat}(T)$ is the saturated vapor pressure, given by the Clausius-Claperon equation. It can be concluded that the heat loss due to material vaporization is:

$$Q_{out}=\dot{m}L_v \tag{5}$$

where L_v is the latent heat of evaporation of SiC.

2.3. Fluid motion and phase field

The process of surface modification and mass removal of SiC by laser is closely related to the phase transition induced by thermal effect, and the hydrodynamic motion of molten material may play a key role in it. Tsai et al. [25] observed an obvious recast layer of micro/nanoporous structure in the surface modification experiment of Ti material by laser, which strongly supports the above view. It is assumed that after the Gaussian distributed pulsed laser acts on the surface of the material, the laser energy density is high enough to cause the solid to liquid to the gas phase transition of the material, accompanied by nucleation, evaporation, and splashing of the molten material. After the laser action ends, the molten liquid reflows and recasts, eventually forming uneven undulations on the surface of the material. The model uses the N–S equation of the incompressible fluid to describe the fluid motion, and uses the

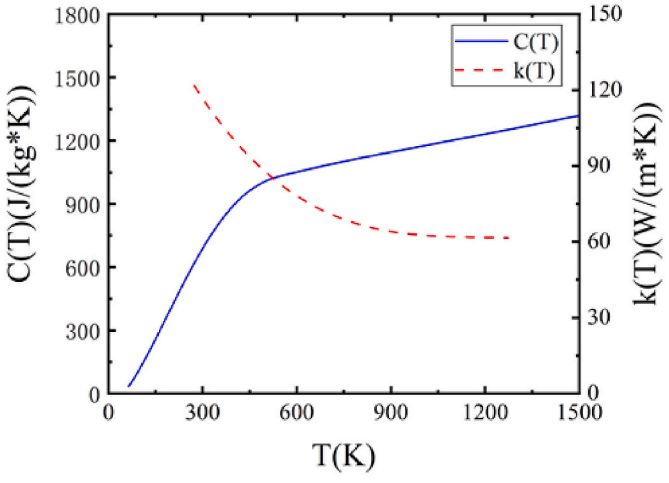

Fig. 2. Variation of thermal conductivity k and specific heat capacity Cp of SiC with temperature.

phase-field equation to track the evolution of the shape, curvature, etc. of the interface of the molten zone over time:

$$\rho\frac{\partial\vec{\mu}}{\partial t}+\rho(\vec{\mu}\bullet\nabla)\vec{\mu}=-\nabla\bullet P+\mu\bullet\nabla\bullet\left(\nabla\vec{\mu}+(\nabla\vec{\mu})^{T}\right)+\rho F$$

$$\frac{\partial\varnothing}{\partial t}+\vec{\mu}\bullet\nabla\varnothing=\nabla\frac{\gamma^{2}\xi}{\varphi^{2}}\nabla\Psi \tag{6}$$

where u is the fluid velocity, $\boldsymbol{\rho}$ and $\boldsymbol{\mu}$ are the density and viscosity of molten SiC respectively, P is the pressure of the flow field, F is the volume force on the fluid domain, φ is the phase field variable, $\boldsymbol{\gamma}$ is the migration adjustment variable, and $\boldsymbol{\xi}$ is mixing energy density, $\boldsymbol{\varphi}$ is the interface thickness control variable. The force on the material in the molten area is divided into body force and surface force. The body force is gravity and thermal buoyancy, and the surface force is surface tension and vaporization recoil force.

The surface tension of the free surface greatly affects the shape and heat transfer of the molten pool interface [26], and the Marangoni effect promotes the flow of molten material from the bottom of the molten pool to both sides, which not only affects the depth and velocity distribution of the molten pool, and transfer heat and mass from the hot area to the cold area. Surface tension and thermocapillary shear force are calculated as follows:

$$\sigma_{n}=\kappa\varepsilon\overline{n}$$

$$\sigma_{\tau}=\epsilon\nabla T\overline{\tau} \tag{7}$$

where $\boldsymbol{\kappa}$ is the free surface curvature and ε is the surface tension coefficient (for liquid SiC is 843 dyne/cm [16]). In addition to surface tension, the recoil pressure of the vapor stream also affects the molten pool movement and the material removal process. The steam recoil pressure on the surface of the melting zone is closely related to the temperature field [27]. When the surface temperature of the material exceeds the boiling point, the recoil pressure is:

$$F_{rp}=0.54P_{sat} \tag{8}$$

where p is the saturated vapor pressure, which is already given in **Eq. (4)**. a, b and c are the surface forces, which are converted into body forces by multiplying the interface function of the phase field variables, and exerted on the vapor/liquid interface in the form of a generalized source term. The overall force of the molten material is shown in Fig. 3. Evaporation should also be considered in the phase-field equation. Therefore, the phase field equation **Eq. 6** is rewritten in this paper.

$$\frac{\partial\Phi}{\partial t}+\vec{u}\bullet\nabla\Phi-\delta(\Phi)\dot{m}\left(\frac{V_{g}}{\rho_{g}}+\frac{V_{1}}{\rho_{1}}\right)=\nabla\bullet\frac{\gamma^{2}\xi}{\varphi^{2}}\nabla\Psi \tag{9}$$

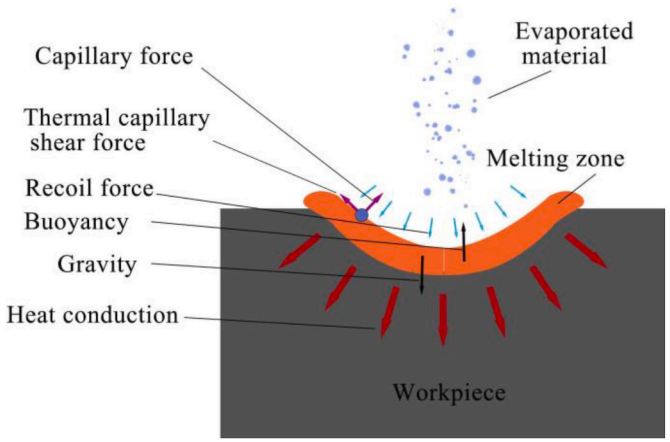

Fig. 3. Force analysis of materials in the molten zone.

where $\dot{m}$ is the mass evaporation rate of SiC, ρ_g and ρ_l are the densities of the gas phase and liquid phase of the SiC material, respectively, and V_g and V_l are the volume fractions of the gas phase and liquid phase in the grid cell in the finite element method.

3. Experimental

Section 3 shows a schematic diagram of the picosecond laser system used in the experiments in this study. The maxi-mum repetition rate of the system is 400 kHz, and the output energy and frequency are adjustable. The beam generated by the laser is linearly polarized light with a pulse width of 10 ps, a wavelength of 1030 nm, and a Gaussian distribution of energy. In the experiment, the laser beam was focused by an electric lens and irradiated vertically on the SiC surface on a two-dimensional precision moving platform. The movement of the scanning galvanometer is precisely controlled by the computer while keeping the working platform fixed, which realizes the line-by-line scanning processing of SiC on a two-dimensional plane (Fig. 4).

In this study, n-type single crystal 4H–SiC produced by Hefei Kejing was used. The slices are of standard orientation (0001), the length and width were both 10 mm, and the thickness was 330 μm. The wafer is single-side polished and the surface roughness Rq of the polished surface is less than 1.5 nm. The Si surface of the SiC sample was cleaned with alcohol before and after the experiment, and then the surface morphology, composition, and mechanical properties of the material were characterized by scanning electron microscopy, white light interferometer, EDS, and nanoindentation. The nanoindenter adopts a load-controlled driving mode, and the maximum indentation load applied to the indenter during the indenter pressing into the sample is preset to 30 mN. To minimize the influence of the creep effect on the measurement accuracy, the indenter will stay at the maximum indentation depth for about 10 s, and then slowly unload. The sample was indented three times under each load to reduce the error, and the interval between each indentation was 100 m to ensure that the points did not affect each other. All experiments in this study were performed in an atmospheric environment.

4. Results and discussion

4.1. The evolution process of temperature and flow fields

When a laser is directed onto the surface of SiC, the energy deposition induces a rapid increase in temperature within the ablated region of the target material. The temperature evolution of the central point on the surface over time, under varying energy densities, is illustrated in

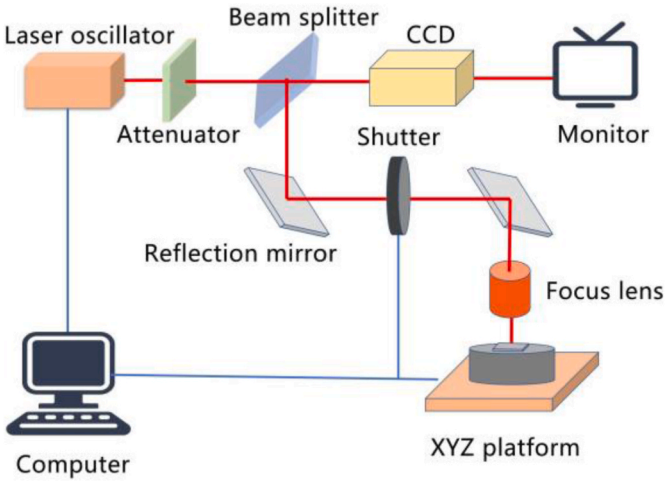

Fig. 4. Schematic diagram of picosecond laser processing equipment.

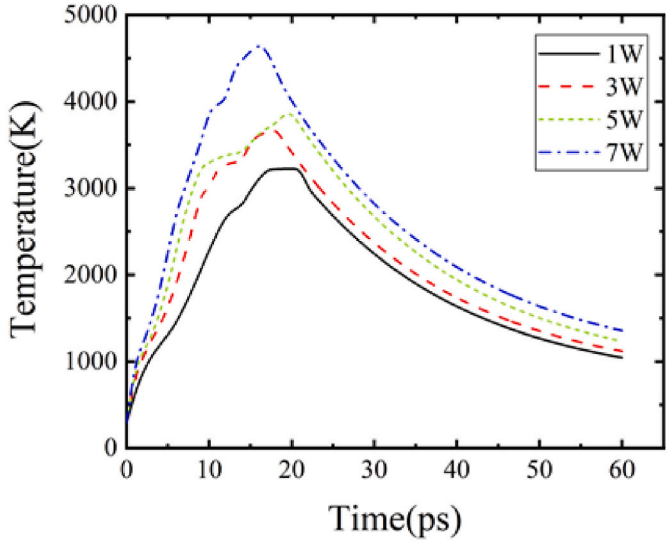

Fig. 5. Variation of surface center temperature with time under different laser power.

Fig. 5. At power levels of 1 W, 3 W, 5 W, and 7 W, the temperature at the central point peaks at 22 ps, 18 ps, 20 ps, and 16 ps, respectively. Higher laser power results in a greater peak temperature and a faster heating rate, as evidenced by the steepness of the curve's slope at the onset. Throughout the entire process of laser irradiation, latent heat of vaporization, convective heat transfer, and thermal radiation play significant roles. In the initial phase, the rate of energy absorption surpasses the rate of heat dissipation, leading to a continuous temperature rise. Due to the Gaussian time distribution of laser energy, the maximum temperature is not attained at the conclusion of the laser pulse but rather when the rate of energy absorption equals the rate of heat dissipation.

The temperature distributions of the ablated regions with different laser fluences are shown in Fig. 6. The pulsed laser energy has a Gaussian distribution in space, so the temperature at the center point is the highest, and the surface temperature of the pit gradually decreases with the increase of the radial distance. There is also a temperature distribution similar to the pit surface along the depth direction, and the temperature gradient in the depth direction is larger. When the temperature of the material reaches the melting point and begins to melt, the temperature gradient inside and on the surface of the molten pool drives the flow of the liquid material to form convection heat transfer, which brings the heat from the surface of the target to the interior and edge of the molten pool, so that the temperature distribution becomes uniform. When the temperature of the material in the molten zone rises to the boiling point, the impurity particles in the molten zone may become vaporization nuclei [28], and then the liquid is violently vaporized around the vaporization nuclei, resulting in a large number of bubbles. Therefore, the formation of micro/nano-porous structures on the SiC surface may be attributed to the generation and collapse of bubbles. The gasification of the material takes away a lot of heat, so the maximum temperature of the material surface is around the gasification temperature.

The flow field distribution in the ablation area under different energy fluences is shown in Fig. 7. It can be seen from the figure that the flow velocity outside the melting zone is the highest. When the energy is 7 W, the flow velocity can reach nearly 200 m/s at 25 ps. Both vaporization of molten material and sputtering caused by flow motion lead to material removal, but the two work in very different ways. During the initial stages of ablation, vaporization dominates. It can be seen from the direction of the vector arrow that the moving speed of the vaporized material is perpendicular to the surface of the material, and there is no lateral shear force. On the contrary, under the action of the thermocapillary force and pressure difference caused by the temperature gradient, the molten droplets flow away from the center of the pit and flow to both sides, thus forming a lateral shearing effect. This is also the reason for the flanging bulge at the edge of the pit. Under the action of the recoil pressure of the high-temperature steam flow, the molten liquid flows from the center to both sides, and the size of the pits on the surface of the target material rapidly expands. The movement of the molten material also causes the size of the dimple to expand, but after the laser action ends, part of the molten liquid is re-cast on the dimpled surface, and the depth and width of the dimple are slightly reduced.

4.2. Surface microstructure evolution

The Gaussian beam is used in the experiment, and the energy of the focused spot decreases step by step according to the Gaussian function from the center to the edge. Under the condition of a scanning speed of 180 mm/s, the effect of different laser energy influences on the surface morphology and microstructure is shown in Fig. 8. When the incident laser power is 1 W, it can be seen from Fig. 8b that many approximately spherical nanoparticles appear on the SiC surface. These nanoparticles are in the form of droplets, with a relatively uniform distribution, and most of them are between 50 and 100 nm in size. A small number of larger particles have a size of nearly 200 nm, which seems to be formed by the aggregation and connection of multiple small-sized particles. When the power of the laser is 3 W, it can be seen from Fig. 8c that both the volume and number of nanoparticles increase, but the arrangement and shape become chaotic and irregular. It is worth noting that these larger particles have reached the micrometer scale, the arrangement assumes a shape similar to that of liquid sputtering, and the boundaries are very clear. As the energy continues to increase, as shown in Fig. 8d–a certain number of micron-sized particles have been aggregated and linked into a sheet-like structure covering the surface of the material (not fully covered). The different sheet-like structures are separated by a deep gully, which shows traces of fluid scouring, oriented at 45° from the lower left to the upper right, showing a weaker periodicity. When the laser fluence reaches 7 W (Fig. 8e), the sheet-like structure in Fig. 8d has also disappeared, each particle has a clear boundary, and the deeper ravines become imperceptible, and the laser energy fluence at this time may be somewhat too large.

Fig. 8f-h shows the SEM images at the energy of 5 w and the scanning speed of 160/140/120 mm/s, respectively. With the same power, a lower sweep speed means more energy deposition per unit area. Therefore, Fig. 8f and d exhibit similar surface structures, while Fig. 8h is similar to Fig. 8e. In Fig. 8g, clear LIPSS has appeared on the left, while the right still appears granular, which is due to the spatial distribution of the pulsed laser energy.

The equivalent pulse number (N) is determined by the beam waist radius (r), repetition frequency (f), and scanning speed (v), and the calculation formula is as follows:

$$N = \sqrt{\frac{\pi}{2}}\frac{rf}{v} \tag{10}$$

Substituting the spot radius of 10 μm, the repetition frequency of 400 kHz, and the scan speed of 140 mm/s into Eq. (10), the equivalent pulse number is about 36. The larger the pulse number N, the smaller the corresponding laser ablation threshold. The dependency between the two is described by **Eq. (11)** [29]:

$$F_{th}(N) = F_{th}(1)N^{\xi-1} \tag{11}$$

where ξ is the material-dependent hatching factor and $F_{th}(1)$ is the threshold flux at $N = 1$. It is calculated that when the number of equivalent pulses is 36, the energy threshold of the LIPSS structure induced in the experiment is 3.98 J/cm^2. Gao et al. [30] used a laser with a wavelength of 1060 nm, a pulse width of 20 ps, and a scanning speed of 200 mm/s to perform ablation experiments on SiC. Using **Eq.**

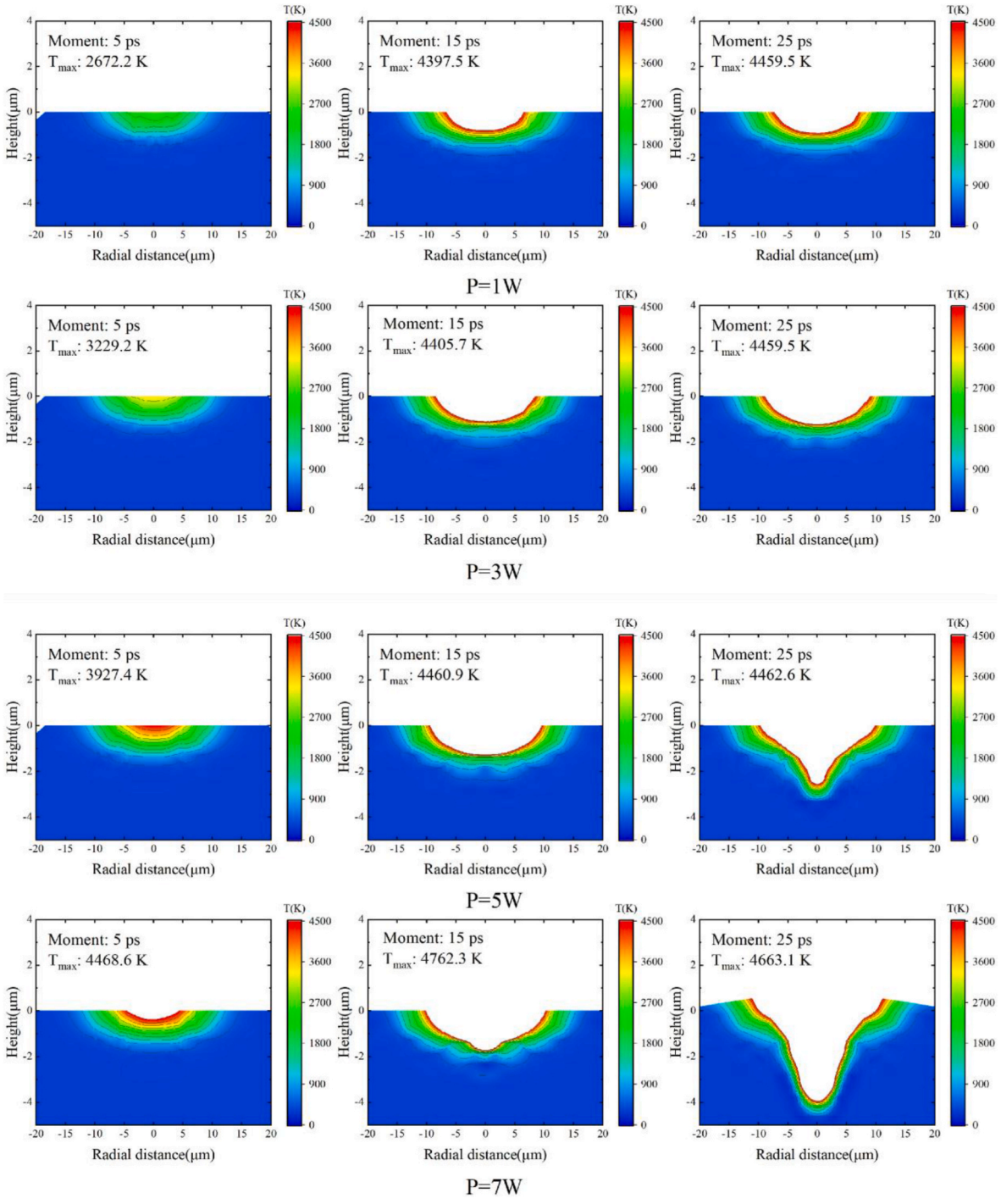

Fig. 6. Evolution of surface temperature field with time under different laser energy fluences.

(10) and Eq. (11), the energy threshold when $N = 36$ was obtained is about 1.27 J/cm^2. S.H.Kim et al. [31] pointed out that surface roughness has a significant effect on the threshold of LIPSS, and smooth surfaces tend to require higher ablation thresh-olds. Since the pulse width and the initial surface roughness of the materials were different between the two experiments, deviations in the ablation threshold were acceptable.

From the SEM images of the SiC surface irradiated by different energy fluences, the surface morphology of SiC has evolved from the formation of nanoparticles to the state of disorder and melting. A plausible explanation for these experimental phenomena is that at lower energy fluences, bound electrons in SiC materials enter excited states by absorbing photons, generating electron-hole pairs. Due to the low hole mobility, the electron-hole pair cannot recombine in a short time. The atoms (holes) from which the electrons are stripped repel each other and gain kinetic energy due to the Coulomb force. These atoms transfer energy to adjacent atoms through collision, and the adjacent atoms continue to collide with their surrounding atoms after receiving energy, causing a Coulomb explosion [32]. The Coulomb explosion leads to atoms sputtering, eventually forming nanoparticles on the surface. At higher energy fluences, electrons can simultaneously absorb multiple photons [33]. The intense emission of electrons destabilizes atomic bonds and further leads to lattice disorder. In addition, the high-density energy deposition causes the material temperature to rise rapidly. The material in the melting zone flows and spreads from the central area to

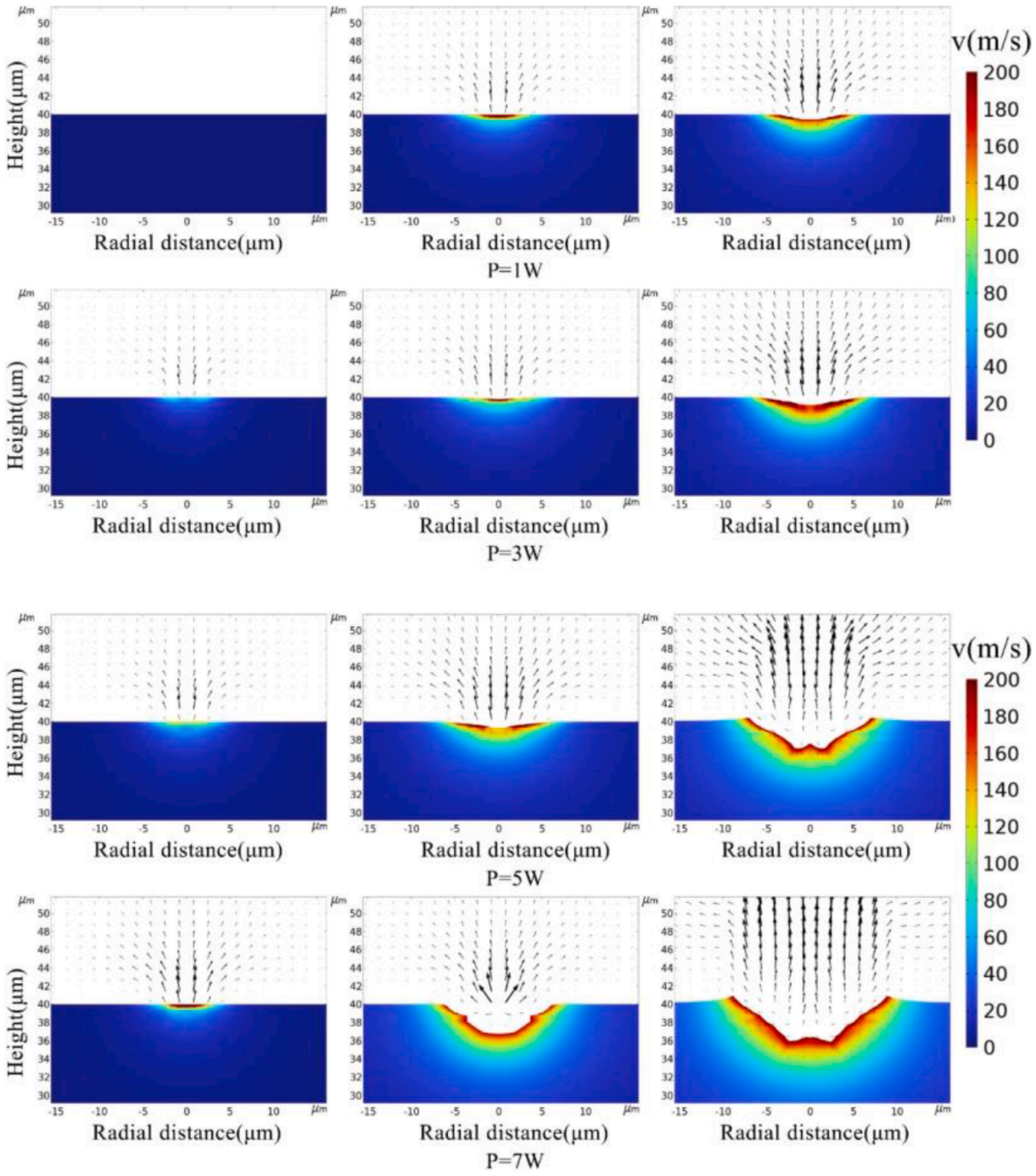

Fig. 7. Variation of fluid velocity with time under different laser energy fluences.

the surrounding areas, the area of the melting zone gradually increases, and the fluid movement begins to dominate. Under the action of multiple pulses, the surface of the material continuously melts and solidifies, which makes the surface veins more blurred, and only clear ravines can be seen at the boundary. When the energy continues to increase, due to the incubation effect [34] and the influence of heat accumulation, the particles and fragments formed by the expansion and fragmentation of the material splash around with the thermal shock wave, so small fragments are randomly distributed on a single stripe appear.

By comparing the surface topography in Fig. 8a-f, it can be seen that laser ablation can change the surface structure of SiC in a large area, but not all changes are beneficial. Non-uniform ablation can lead to deeper

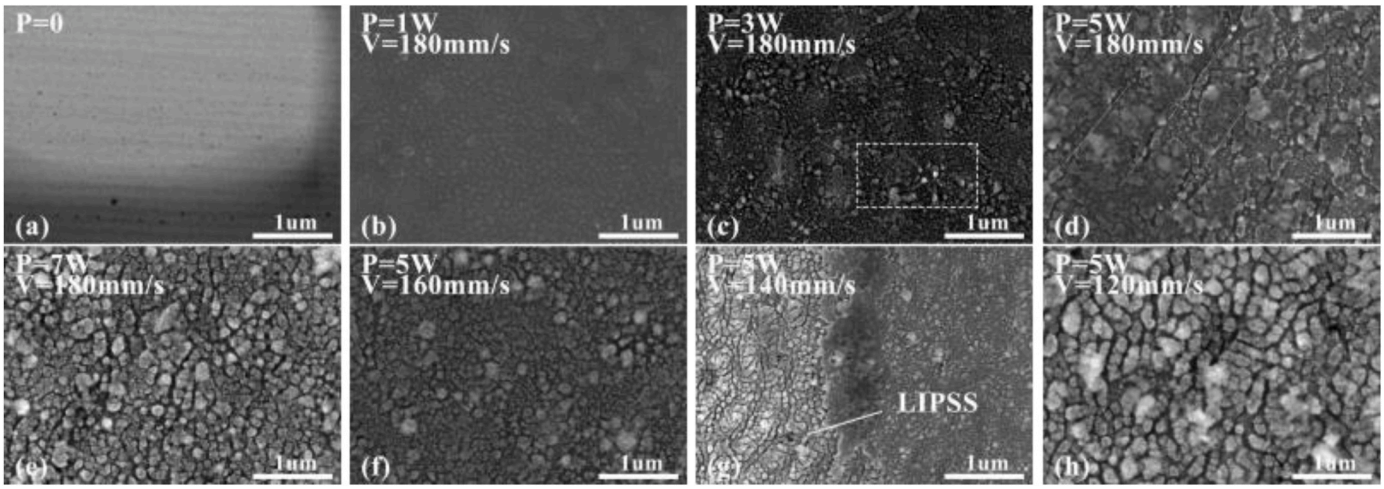

Fig. 8. Surface topography at different laser fluences and scanning speeds: (a–e) different laser energies, (d, f-h) different scanning speeds.

defects, which in turn reduce polishing efficiency. To further explore the effect of laser ablation on the surface profile of the material, white light interferometer measurements were carried out.

4.3. Surface quality and profile

Fig. 9 shows the 3D microscopic surface morphologies of SiC under different laser energy fluences, where Ra is the arithmetic mean deviation of the contour, and Rq is the root mean square roughness. It can be seen from Fig. 10 that when the laser power increases from 1 W to 3 W,

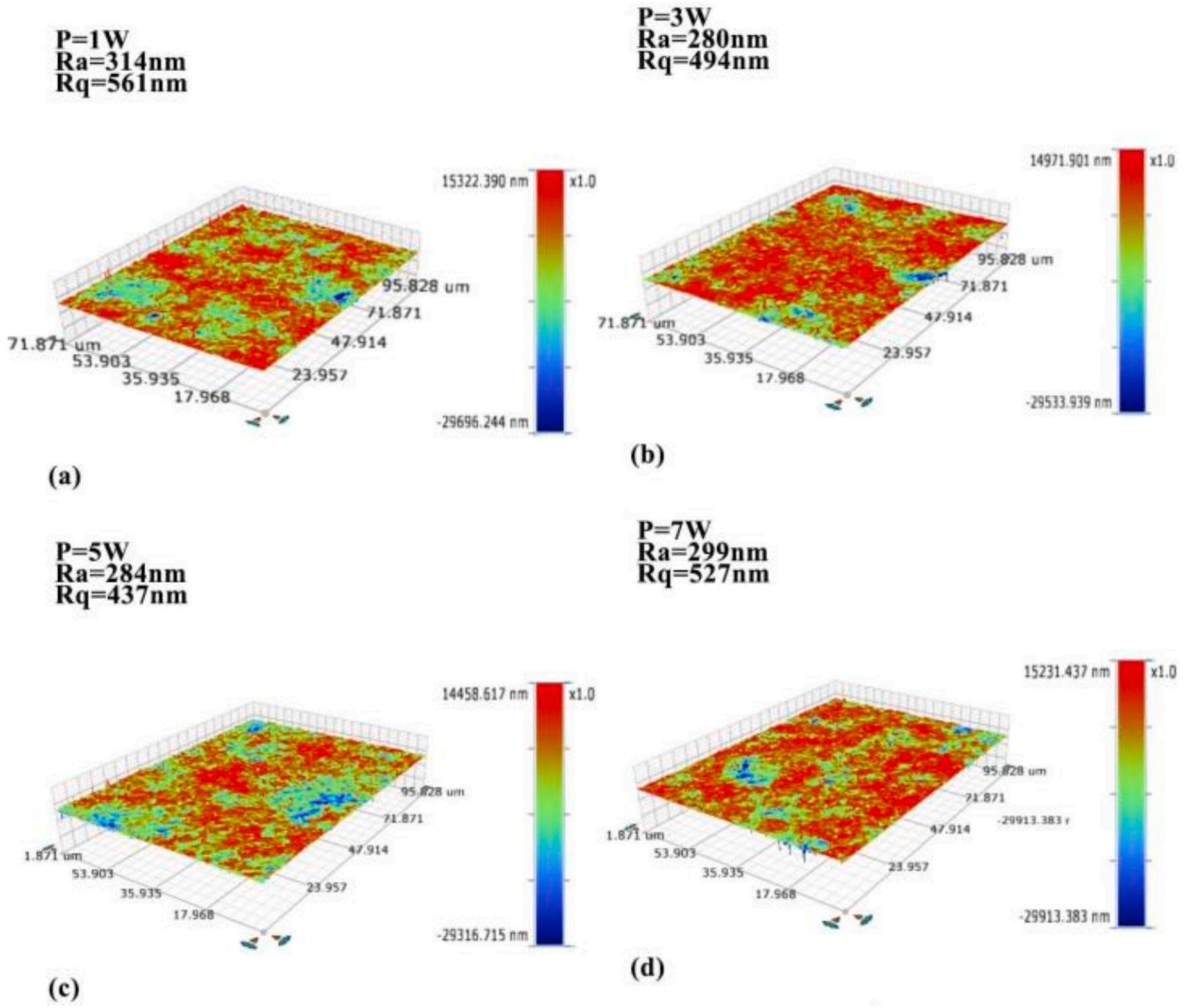

Fig. 9. Three dimensional surface topography under different laser energy.

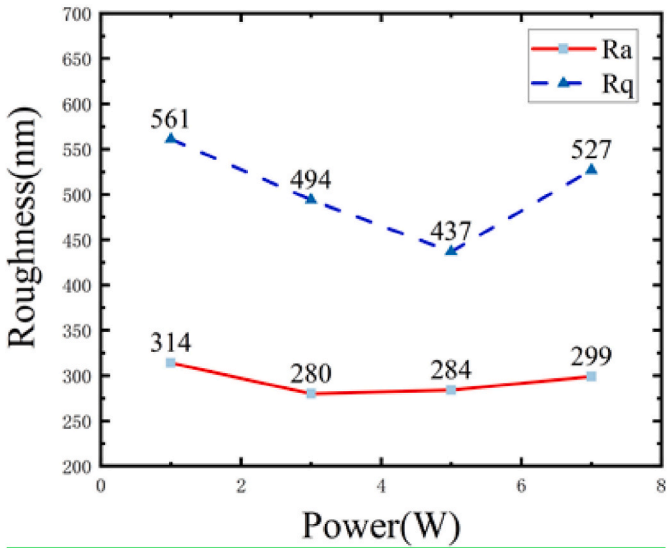

Fig. 10. Surface roughness under different laser energy.

the Ra on the surface of the material decreases from 314 nm to 280 nm, the Rq decreases from 561 nm to 494 nm, and the surface quality of the material is greatly improved. This may be due to the higher temperature melting the peaks of the surface as the energy builds up, and the molten material flows into the valley areas, thereby flattening the surface. As the power increases to 5 W, Ra has almost no change, but Rq maintains an approximate linear decreasing trend. But when the power increased to 7 W, the Ra and Rq of the workpiece surface begin to increase, and the surface quality begin to decline. This may be attributed to the plasma shielding effect [35]. Higher energies lead to evaporation and ionization of the material, and the evaporated material rapidly expands into a hemisphere above the surface, absorbing most of the laser energy through the inverse bremsstrahlung and photoionization processes [36]. As the fluid movement in the melting zone is suppressed, coupled with the recasting of the evaporated material, the surface undulations of the material increase instead.

During the pulsed laser's action, sputtering and vaporization cause material removal. Due to the presence of recoil pressure and surface tension, the liquid phase material flows to the edge of the melting zone, forming a hump at this location. After the action of the pulsed laser is over, the molten liquid material on the wall of the pit cools and reflows, and finally, a crater-like surface is formed in the ablation area. The experiment uses a white light interferometer to capture the profile features of the grooves, which are roughly V- shaped or U-shaped. Due to the recasting phenomenon of the material, the obtained profile data fluctuate greatly, so the maximum groove depth is used for comparison in the model verification.

Fig. 11 shows the trend of groove depth increasing with laser power. When the power is 1 W, it can be seen that the simulation result of the groove depth is slightly smaller than the experimental result. This is due to heat accumulation at smaller energies, which enhances the material removal process [37] and is ignored in the simulations for efficient computation. Conversely, at higher laser power, the simulated groove depth is higher than that obtained from the experiment, which may be attributed to the higher energy loss in the experiment. At higher energy fluence, the heating process of the material is more intense, and the plasma shielding and fluid motion on the surface will consume more energy. Since the shielding and absorption of laser energy by the plasma are ignored in the basic assumptions of the simulation, the groove depth values obtained at high energy fluences are on the high side. Due to the recasting of the gas phase material in the experiment, the groove width in the experiment is always slightly lower than the simulation results, but overall good agreement is achieved, and the groove width is close to the spot diameter of the laser. Therefore, the heat-flow coupling model in this paper is helpful to understand the material removal process of ps laser processing SiC.

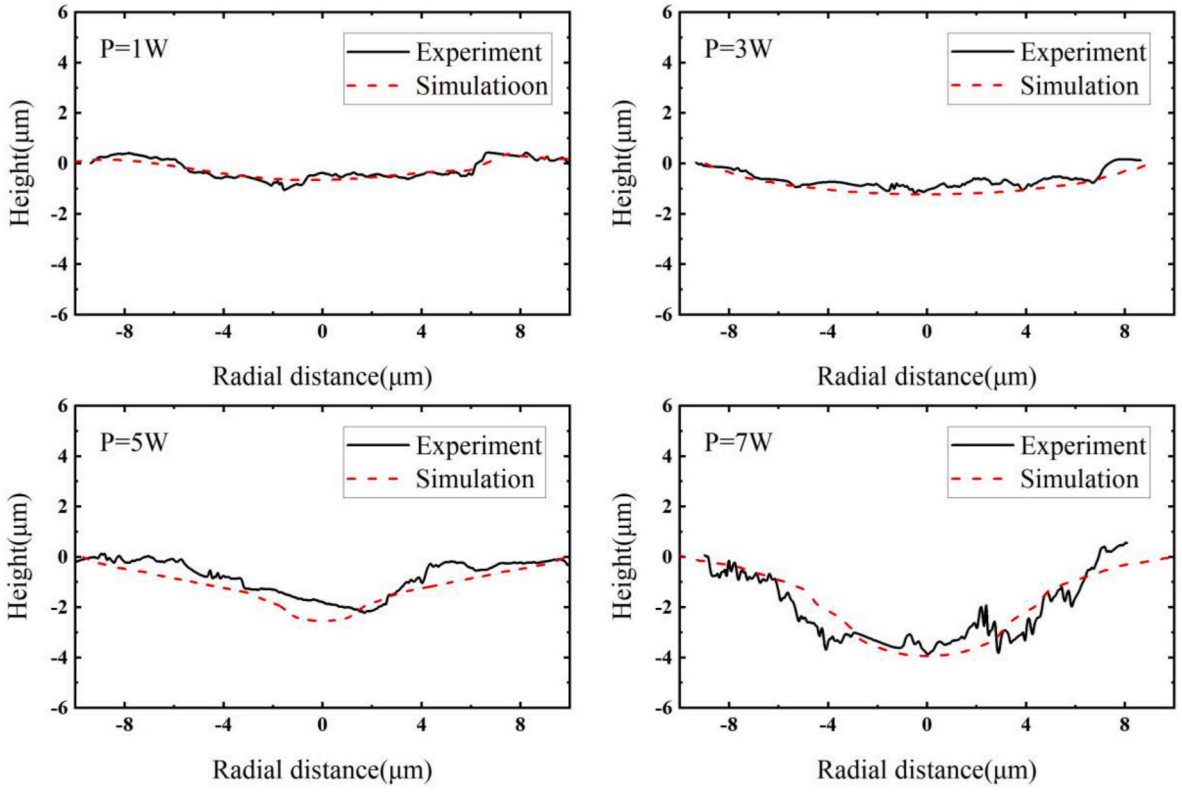

Fig. 11. Comparison of simulation and experimental profiles under different laser energies.

4.4. Material composition and mechanical properties analysis

The modification of SiC by picosecond laser is accompanied by complex physical and chemical changes, and the mechanical properties of the modified surface are very important to the CMP process. For this reason, EDS analysis and nanoindentation experiments are employed in this paper. Fig. 12 shows the ratio of elemental content changes with different laser energies. It can be found that the elemental ratio of silicon to carbon is nearly identical when the laser energy is equal to 1 W. With the increase of energy, the proportion of oxygen element and Si element increases, which indicates that oxygen participates in the photochemical reaction on the SiC surface. The content of element C showed a trend of first increase and then a slight decrease, which is similar to the trend of surface roughness in Fig. 11, and both may be due to the same reason (plasma shielding effect). The photochemical reactions on the SiC surface under picosecond laser irradiation mainly include the following processes:

$$\begin{aligned} 3O_2 + 2SiC &= 2SiO_2 + 2CO \\ 2O_2 + SiC &= SiO_2 + CO_2 \\ 2CO + O_2 &= 2CO_2 \end{aligned} \tag{12}$$

The SiO_2 generated by the oxidation of Si can be recast on the surface of the workpiece after cooling, while the C element can only be separated from the surface of the workpiece in the form of CO_2 gas. Therefore, the content of the Si element is similar to that of the C element at first, and then gradually becomes higher than that of the C element as the oxidation reaction proceeds. SiO_2 has a Mohs hardness of 7, which is lower than that of SiC (9.5) and can be easily removed during polishing. The SiC processed by laser irradiation consists of a surface deposition layer, subsurface defect layer, and matrix. The deposition layer mainly includes the LIPSS layer and the recast layer, and the subsurface defect layer is mainly residual stress and cracks. The CMP process must completely remove the influence of mechanical properties of the modified SiC surfaces. The nanohardness of the sample is calculated as follows:

$$H = \frac{P_{max}}{A} \tag{13}$$

in the formula, P_{max} is the maximum load, and A is the projected area of the indentation. According to the Oliver- Pharr method [38], the reduced elastic modulus Er can be determined from the data of the complete loading/unloading cycle. The reduced elastic modulus is expressed as:

$$E_r = \frac{\sqrt{\pi}}{2}\frac{S}{\sqrt{A}} \tag{14}$$

The two to obtain a high-quality surface at the atomic level. Nanoindentation experiments were performed to obtain the where E_r is the reduced elastic modulus, S is the stiffness, and A is the projected area of the indentation. The value of the elastic modulus of the tested material can be obtained by **Eq. (15)**:

$$\frac{1}{E_r} = \frac{1-\nu^2}{E} + \frac{1-\nu^2}{E_i} \tag{15}$$

where υ and E are the Poisson's ratio and elastic modulus of the tested material, and ν_i and E_i are those of the diamond indenter, which are 1141 GPa and 0.07, respectively.

The measured load-depth curves of the material at different energy fluences are shown in Fig. 13. The nanoindentation depth and deformation recovery behavior vary with different regions of the melt pool.

The nanohardness and elastic modulus values calculated from the measurements are shown in Fig. 14. It can be seen that the nanohardness and elastic modulus of the material show an overall downward trend with the increase of energy. The nanohardness (3.16 GPa) of the material when the laser energy is 7 W is reduced to 37% of that at 1 W (8.45 GPa), and the elastic modulus is reduced to 103.82 GPa, which is much lower than that of 4H–SiC (347 GPa) [39]. In addition, a 'pop-in' event using the following formula [40]:

$$\tau = 0.47\frac{P}{\pi R h} \tag{16}$$

where P is the indenter load, R is the indenter radius, and h is the indentation depth. After calculation, the shear stress at this point is 17.25 GPa, which is lower than the theoretical shear strength value of 4H–SiC (20.9 GPa) [39]. This indicates that the microstructure and phase of the material have changed, and the mechanical properties of the material have decreased significantly, which will increase the material removal rate of the polishing process.

5. Conclusion

A multi-scale coupled model based on optical carrier absorption, thermal conduction, thermal radiation, and phase transition resolidification process was established to study the laser ablation process of

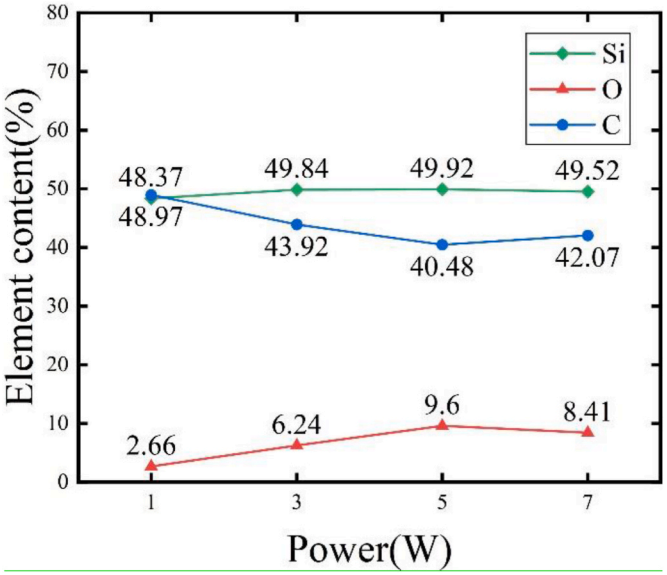

Fig. 12. The elemental content ratios change with varying laser energy.

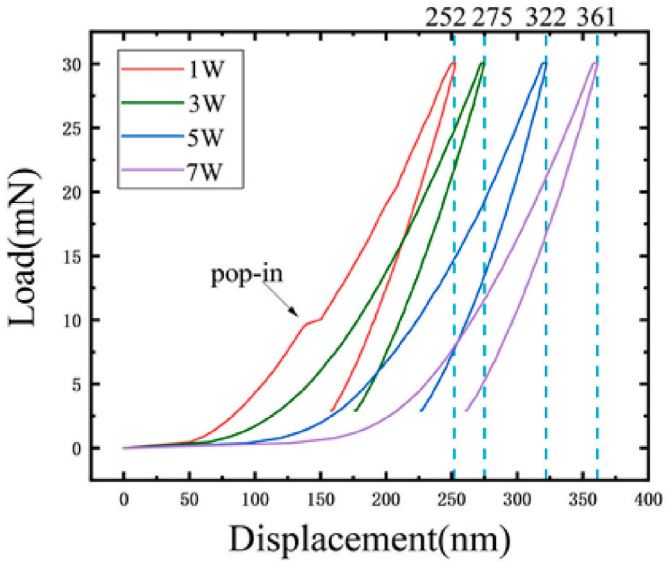

Fig. 13. Load-displacement curves at different energies.

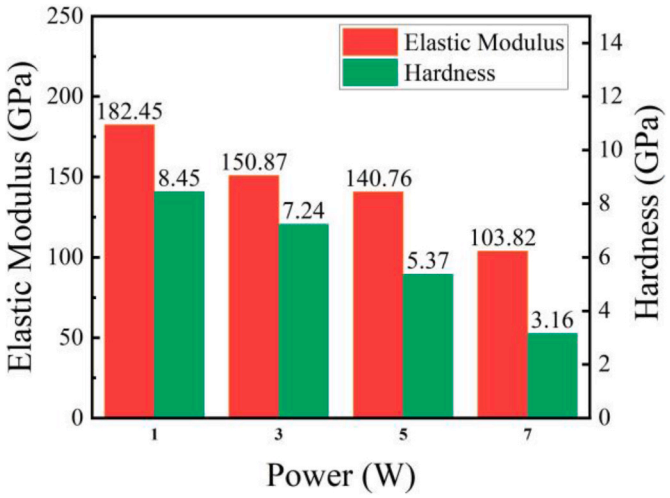

Fig. 14. Elastic modulus and hardness at different energies.

SiC. The simulation results show that:

a) The recoil action of the vaporized material does not have lateral shear force. The hump generated at the edge of the pit is mainly caused by surface tension, and the formation of the micro/nano porous structure on the SiC surface is attributed to the generation and rupture of bubbles.
b) At low flux, the simulated results of the groove depth are lower than the experimental results due to the existence of the heat storage mechanism. while at high flux, the opposite is true, which is attributed to the energy decay during the experiment.

The action of pulsed laser on SiC material involves complex physical and chemical changes. In the experiment, lasers with different energy fluences were used to irradiate the SiC surface, and the modification mechanism was mainly explored from the aspects of surface microstructure, surface quality, composition analysis, and mechanical properties. Experimental results show that:

c) With increasing energy, the surface topography of SiC transitions from nanoparticle formation to disorder to a melting state. At lower energy fluence, the effect of laser on SiC is based on Coulomb explosion. When the energy increases, the material expands and breaks to form LIPSS due to the multiphoton absorption, incubation effect, and heat accumulation. The experimentally measured ablation threshold of LIPSS is 3.98 J/cm^2, which is higher than 1.27 J/cm^2 in the reference, because the SiC slices used in this experiment have a smoother initial surface.
d) The flow of the molten liquid makes the surface flatter, and the lowest Ra (437 nm) is obtained under the laser energy of 5 W when the scanning speed is 180 mm/s. The relationship between the surface quality and the energy fluence is not linear, and holes may appear at higher energies.
e) EDS results indicate that oxygen participates in the photochemical reaction of laser to SiC, and the generated SiO_2 significantly reduces the surface hardness. The elastic modulus of the surface at 7 W measured by the nanoindentation experiment is 103.82 GPa, the surface hardness is 3.16 GPa, and the shear stress at PoP-in is 17.25 GPa. The laser action changed the microstructure and phase of the SiC surface, and the modified surface had lower mechanical strength.

Declaration of competing interest

The authors declare that they have no known competing financial interests or personal relationships that could have appeared to influence the work reported in this paper.

Acknowledgements

This work was supported by the National Natural Science Foundation of China (No. 52205478), Basic Research Programs of Natural Science Foundation of Jiangsu Province (No. BK20220891), National Key Laboratory of Science and Technology on Helicopter transmission (No. HTL-A-22G04), and China Postdoctoral Science Foundation Special Funding (No. 2022TQ0153).

References

[1] Deng H, Ueda M, Yamamura K. Characterization of 4h-sic (0001) surface processed by plasma-assisted polishing. Int J Adv Des Manuf Technol 2014;72:1–7.
[2] Everson W, Snyder D, Heydemann V. Polishing and surface characterization of sic substrates. In: Materials science forum. Zurich-Uetikon, Switzerland: Trans Tech Publications Ltd.; 2000. p. 837–40.
[3] Yamamura K, Emori K, Sun R, Ohkubo Y, Endo K, Yamada H, Chayahara A, Mokuno Y. Damage-free highly efficient polishing of single-crystal diamond wafer by plasma-assisted polishing. CIRP Annals 2018;67:353–6.
[4] Deng H, Hosoya K, Imanishi Y, Endo K, Yamamura K. Electro-chemical mechanical polishing of single-crystal sic using ceo2 slurry. Electrochem Commun 2015;52:5–8.
[5] Zhu JT, Lu JB, Pan JS, Yan QS, Xu XP. Study of cluster magnetorheological-chemical mechanical polishing technology for the atomic scale ultra-smooth surface planarization of sic. In: Advanced materials research. Trans Tech Publ; 2013. p. 284–90.
[6] Chen Ni, Liu Jiawei, He Ning, Xiao Xingzhi, Zhao Junyi, Jia Yibo, Yu Nan. Fabrication of high aspect ratio grooves on aluminium nitride by laser and chemical milling enhanced micro milling. J Mater Process Technol 2024;325:118299.
[7] Birnbaum M. Semiconductor surface damage produced by ruby lasers. J Appl Phys 1965;36:3688–9.
[8] Meng B, Zheng J, Yuan D, Xu S. Machinability improvement of silicon carbide via femtosecond laser surface modification method. Appl Phys A 2019;125:1–12.
[9] Dufft D, Rosenfeld A, Das S, Grunwald R, Bonse J. Femtosecond laser-induced periodic surface structures revisited: a comparative study on zno. J Appl Phys 2009;105:034908.
[10] Obara G, Shimizu H, Enami T, Mazur E, Terakawa M, Obara M. Growth of high spatial frequency periodic ripple structures on sic crystal surfaces irradiated with successive femtosecond laser pulses. Opt Express 2013;21:26323–34.
[11] Molian P, Pecholt B, Gupta S. Picosecond pulsed laser ablation and micromachining of 4h-sic wafers. Appl Surf Sci 2009;255:4515–20.
[12] Wang C, Kurokawa S, Doi T, Yuan J, Sano Y, Aida H, Zhang K, Deng Q. The polishing effect of sic substrates in femtosecond laser irradiation assisted chemical mechanical polishing (cmp). ECS Journal of Solid State Science and Technology 2017;6:P105.
[13] Xie X, Peng Q, Chen G, Li J, Long J, Pan G. Femtosecond laser modification of silicon carbide substrates and its influence on cmp process. Ceram Int 2021;47:13322–30.
[14] Yuan P, Gu D, Dai D. Particulate migration behavior and its mechanism during selective laser melting of tic reinforced al matrix nanocomposites. Mater Des 2015;82:46–55.
[15] Sciti D, Bellosi A. Laser-induced surface drilling of silicon carbide. Appl Surf Sci 2001;180:92–101.
[16] Samant AN, Daniel C, Chand RH, Blue CA, Dahotre NB. Computational approach to photonic drilling of silicon carbide. Int J Adv Des Manuf Technol 2009;45:704–13.
[17] Wang C, Kurokawa S, Doi T, Yuan J, Lv B, Zhang K. Surface morphology evolution induced by multiple femtosecond laser ablation on 4h-sic substrate and its application to cmp. ECS Journal of Solid State Science and Technology 2017;6:P853.
[18] Huseynov EM, Naghiyev TG. Study of thermal parameters of nanocrystalline silicon carbide (3C-SiC) using DSC spectroscopy. Appl Phys A 2021;127(4):267.
[19] Huseynov EM, Naghiyev TG, Aliyeva US. Thermal parameters investigation of neutron-irradiated nanocrystalline silicon carbide (3C–SiC) using DTA, TGA and DTG methods. Phys B Condens Matter 2020;577:411788.
[20] Huseynov EM, Naghiyev TG, Aliyeva US. Thermal parameters investigation of neutron-irradiated nanocrystalline silicon carbide (3C–SiC) using DTA, TGA and DTG methods. Phys B Condens Matter 2020;577:411788.
[21] Yan Bo, Chen Ni, Zhu Yan, Yang Yinfei, Zhao Guolong, Zhao Wei, Xiuqing Hao, Liang Li, Wang Lei, Abele Eberhard, He Ning. Instantaneous formation of covalently bonded diamond–graphite–graphene with synergistic properties. Int J Mach Tool Manufact 2023;193:104087.
[22] Chen Ni, Zhao Junyi, Wang Runkai, Yan Bo, Wu Yang, Li Liang, Yu Nan, He Ning. Inhibition effect of covalent carbon nanosheets on mechanochemical wear of diamond. Mater Des 2024;237:112573.
[23] Mao SS, Mao X, Greif R, Russo RE. Initiation of an early-stage plasma during picosecond laser ablation of solids. Appl Phys Lett 2000;77:2464–6.
[24] Bhushan B, Gupta BK. Handbook of tribology: materials, coatings, and surface treatments. 1991.

[25] Tsai MH, Haung CF, Shyu SS, Chou YR, Lin MH, Peng PW, Ou KL, Yu CH. Surface modification induced phase transformation and structure variation on the rapidly solidified recast layer of titanium. Mater Char 2015;106:463–9.
[26] Han L, Liou FW, Musti S. Thermal behavior and geometry model of melt pool in laser material process. 2005.
[27] Cho WI, Na SJ, Thomy C, Vollertsen F. Numerical simulation of molten pool dynamics in high power disk laser welding. J Mater Process Technol 2012;212:262–75.
[28] Sundaram S, Mazur E. Inducing and probing non-thermal transitions in semiconductors using femtosecond laser pulses. Nat Mater 2002;1:217–24.
[29] Bonse J, Baudach S, Krüger J, Kautek W, Lenzner M. Femtosecond laser ablation of silicon–modification thresholds and morphology. Appl Phys A 2002;74:19–25.
[30] Gao B, Guo D, Zhang X, Chen G, Pan G. Picosecond laser-assisted chemical mechanical polishing (cmp): aiming at the si- face of single-crystal 6h-sic wafer. ECS Journal of Solid State Science and Technology 2021;10:044008.
[31] Kim S, Byun K, Sohn I, Jeong S. Progressive formation of fine and coarse ripples on sic surface by repeated irradiation of femtosecond laser pulses. Appl Phys B 2013;113:395–402.
[32] Terasawa M, Insepov Z, Sekioka T, Valuev A, Mitamura T. Sputtering due to coulomb explosion in highly charged ion bombardment. Nucl Instrum Methods Phys Res Sect B Beam Interact Mater Atoms 2003;212:436–41.
[33] Kudryashov S, Danilov P, Startseva E, Ionin A. Multi- zone single-shot femtosecond laser ablation of silica glass at variable multi-photon ionization paths. JOSA B 2018;35:B38–42.
[34] Ehrhardt M, Raciukaitis G, Gecys P, Zimmer K. Mi- crostructuring of fused silica by laser-induced backside wet etching using picosecond laser pulses. Appl Surf Sci 2010;256:7222–7.
[35] Yan Z, Mei X, Wang W, Pan A, Lin Q, Huang C. Numerical simulation on nanosecond laser ablation of titanium considering plasma shield and evaporation-affected surface thermocapillary convection. Opt Commun 2019;453:124384.
[36] Zhou Y, Tao S, Wu B. Backward growth of plasma induced by long nanosecond laser pulse ablation. Appl Phys Lett 2011;99:051106.
[37] Zhu H, Zhang Z, Xu J, Ren Y, Zhu Z, Xu K, Wang Z, Wang C. A numerical study of picosecond laser micro-grooving of single crystalline germanium: mechanism discussion and process simulation. J Manuf Process 2021;69:351–67.
[38] Oliver WC, Pharr GM. An improved technique for determining hardness and elastic modulus using load and displacement sensing indentation experiments. J Mater Res 1992;7:1564–83.
[39] Zhao X, Langford RM, Shapiro IP, Xiao P. Onset plastic deformation and cracking behavior of silicon carbide under contact load at room temperature. J Am Ceram Soc 2011;94:3509–14.
[40] Goel S, Yan J, Luo X, Agrawal A. Incipient plasticity in 4h-sic during quasistatic nanoindentation. J Mech Behav Biomed Mater 2014;34:330–7.